J. Fluid Mech. (2014), *vol.* 748, *pp.* 932–956. © Cambridge University Press 2014
doi:10.1017/jfm.2014.212

Dynamics of revolving wings for various aspect ratios

D. J. Garmann† and M. R. Visbal

Air Force Research Laboratory, Wright–Patterson AFB, OH 45433, USA

(Received 30 September 2013; revised 28 February 2014; accepted 12 April 2014;
first published online 12 May 2014)

High-fidelity, direct numerical simulations (DNSs) are conducted to examine the vortex structure and aerodynamic loading of unidirectionally revolving wings in quiescent fluid. Wings with aspect ratios (AR) = 1, 2 and 4 are considered at a fixed root-based Reynolds number of 1000. Each wing is shown to generate a coherent leading-edge vortex (LEV) that remains in close proximity to the surface and provides persistent suction throughout the motion. Towards the tip, the LEV lifts off as an arch-like structure and reorients itself along the chord through its connection with the tip vortex. The substantial and sustained aerodynamic loads achieved during the motion saturate with aspect ratio resulting from the chordwise growth of the LEV along the span eventually becoming geometrically constrained by the trailing edge. Further, for $AR = 4$, substructures develop in the feeding sheet of the LEV, which appear to directly correlate with the local, span-based Reynolds number achieved during rotation. The lower-aspect-ratio wings do not have sufficient spans for these transitional elements to manifest. In contrast, vortex breakdown, which occurs around midspan for each aspect ratio, shows a strong dependence on the spanwise pressure gradient established between the root and tip of the wing and not local Reynolds number. This independent development of shear-layer substructures and vortex breakdown parallels very closely with what has been observed in delta wing flow. Next, the centrifugal, Coriolis and pressure gradient forces are also analysed at several spanwise locations across each wing, and the centrifugal and pressure gradient forces are shown to be responsible for the spanwise flow above the wing. The Coriolis force is directed away from the surface at the base of the LEV, indicating that it is not a contributor to LEV attachment, which is contrary to previous hypotheses. Finally, as a means of emphasizing the importance of the centrifugal force on LEV attachment, the $AR = 2$ wing is simulated with the addition of a source term in the governing equations to oppose and eliminate the centrifugal force near the surface. The initial formation and development of the LEV is unhindered by the absence of this force; however, later in the motion, the outboard lift-off of the LEV moves inboard. Without the opposing outboard-directed centrifugal force to keep the separation past midspan, the entire vortex eventually separates and moves away from the surface.

Key words: low-Reynolds-number flows, vortex breakdown, vortex flows

† Email address for correspondence: daniel.garmann.1.ctr@us.af.mil

https://doi.org/10.1017/jfm.2014.212 Published online by Cambridge University Press

1. Introduction

While the aerodynamics of flapping wings have been heavily studied in recent years, there is still much about the many complex mechanisms of biological flight that is poorly understood. At relatively low speeds or even hover, flapping flight can engender a broad range of difficult-to-predict, unsteady flow phenomena such as vortex breakdown and transition. The extensive range of pitching and plunging amplitudes can also induce large-scale vortex interactions that can dramatically impact performance and stability. In an attempt to quantify the complex aerodynamics of insect flight, several experimental studies have been presented by Dickinson (1994), Ellington (1999), Usherwood & Ellington (2002*a*), Usherwood & Ellington (2002*b*), Sane (2003), Birch & Dickinson (2003), Lehmann (2004) and Lehmann & Pick (2007). These works provide insight into the dominant mechanisms of lift enhancement for flapping wing flight produced from leading edge and tip vortex formation coupled with wing–wake/wing–wing interactions to create dynamic stall-like effects and favourable upwash/downwash that allow biological fliers such as birds and insects to sustain flight and maneuver. Excellent reviews of bio-inspired aerodynamics are provided by Shyy *et al.* (2008) and Shyy *et al.* (2013).

The dynamic stall effect resulting from sustained leading-edge vortex (LEV) attachment has been examined by many researchers through experiments and computations of reciprocating or unidirectionally rotating wings. The experiments of Birch, Dickson & Dickinson (2004) show the formation of an attached LEV with no trailing edge shedding at very large angles of rotation (270°). This was observed over a range of Reynolds numbers ($120 \leqslant Re \leqslant 1400$) despite differences in flow structure, where increased Reynolds number promotes a helical flow pattern in the axial direction within the core of the LEV. Poelma, Dickson & Dickinson (2006) found similar results in their experiments and observed significant spanwise flow around the wing suggesting that it leads to stability of the LEV by draining circulation from the wing and balancing the vorticity generated by the leading edge as first put forth by Ellington *et al.* (1996). Substantial and widespread spanwise flow was also observed in the experiments of Kim & Gharib (2010), where the authors attributed it to the pressure gradient and tilted vorticity of the LEV as it increases in size from root to tip. The results of Lentink & Dickinson (2009*a*,*b*) further support the assertion that spanwise flow balances the formation of vorticity at the leading edge by transporting it towards the tip. They further postulate that Coriolis acceleration is equally important for the attachment of the LEV; however, this claim has become a point of contention within the literature. Ansari *et al.* (2009) experimentally investigated a rotating wing of $AR = 2.5$, impulsively started from rest and accelerated to constant rotation-based Reynolds numbers of $Re = 500$ and 15 000. A coherent and attached LEV was observed from the root to around 70 % span with substantial spanwise flow across that section of the wing that was of the order of 80 % of the wingtip speed. The higher-Reynolds-number flow also showed the resemblance of Kelvin–Helmholtz instabilities in the LEV feeding sheet. The assertion of spanwise vorticity transport inhibiting LEV shedding is reiterated in the works of Mao & Jianghao (2004), where they suggest the spanwise flow is provided by the pressure gradient established between the root and tip of the wing.

Ozen & Rockwell (2012*a*,*b*) offer detailed experimental volume reconstruction of the flow around a rotating plate. A coherent and attached LEV that is connected with the tip, trailing-edge and root vortices to form a continuous loop that was observed throughout the wing's motion. Similarly, Carr, Chen & Ringuette (2013) examined the effects of aspect ratio for an impulsively started, revolving wing configuration at

https://doi.org/10.1017/jfm.2014.212 Published online by Cambridge University Press

a tip-based Reynolds number of $Re = 5000$ using stereoscopic digital particle image velocimetry (SDPIV). The excellent experimental flow visualizations for wings of $AR = 2$ and 4 reveal coherent and attached LEVs that are initially connected to their respective tip and trailing-edge vortices as loop structures. Each LEV eventually lifts off near the wingtip and becomes arch-like with the higher-aspect-ratio wing's LEV moving farther aft, causing the formation of secondary vortices ahead of the primary vortex. These secondary structures were also observed in the computational work of Harbig, Sheridan & Thompson (2013) for various aspect ratios and Reynolds numbers. The authors of that study also suggest using the wing span as the characteristic length of rotating wings to decouple Reynolds number and aspect ratio effects. Cheng *et al.* (2013) also analysed the three-dimensional flow structure and vorticity transport associated with a rotating wing of $AR = 7$ and $Re = 200$ using volumetric three-component velocimetry (V3V). At such a low Reynolds number, significant vorticity was convected into the wake and downward from the induced downwash of the tip vortex, and interestingly, the results showed little-to-no spanwise vorticity transport.

A revolving wing of $AR = 1$ was simulated using high-fidelity, large eddy simulations (LES) by Garmann, Visbal & Orkwis (2013*b*). This work detailed the vortex formation and attachment across a very broad range of rotational-based Reynolds numbers ($200 \leqslant Re \leqslant 60\,000$) along with the accompanying aerodynamic loads. It was determined that for the Reynolds numbers examined, the overall vortex structure including the attachment of a LEV was mostly insensitive to transitional effects despite the apparent vortex breakdown and shear layer instabilities observed at higher Reynolds numbers. The higher-Reynolds-number flows did augment force production on the wing, although the growth of the force components saturated for $Re > 2000$. The Coriolis force in and around the LEV was also examined for each Reynolds number and shown to be directed away from the wing surface, indicating that Coriolis does not contribute to vortex attachment for the aspect-ratio-one wing. Comparisons of the midspan velocity and vorticity contours at several rotational angles were made with available experimental PIV measurements (Ozen & Rockwell 2012*a*), and very favourable agreement was found.

While a broad body of work exists on revolving and flapping wings, higher-resolution experimental and computational investigations must still be conducted to provide further insights into the complex three-dimensional vortical interactions and transitional processes incurred. The purpose of the present high-fidelity computational study is to examine the three-dimensional flow structure and aerodynamic loading generated by revolving wings of various aspect ratios to build upon the recent work by the current authors that detailed the flow over an aspect-ratio-one wing (Garmann *et al.* 2013*b*). Wings of $AR = 1$, 2 and 4 will be simulated using a high-order, implicit large eddy simulation (ILES) approach to examine vortex breakdown and shear-layer instabilities associated with the attached LEV. In addition, the importance of centrifugal force on LEV attachment will be assessed by simulating a revolving wing with the addition of a source term in the governing equations to oppose and eliminate the rotational force near the wing surface. This is in an effort to isolate the dynamic effects due to rotation and determine their impact on the resulting flow structure.

The remainder of this document is as follows: the governing equations and numerical technique are outlined in the next two sections followed by a description of the revolving wing set-up. Next, the effects of aspect ratio on the unsteady flow structure and aerodynamic loads are described along with an examination of the

https://doi.org/10.1017/jfm.2014.212 Published online by Cambridge University Press

dynamic forces due to rotation and how they correlate with LEV attachment. Finally, a simulation of a revolving wing with the addition of a source term in the governing equations to selectively eliminate the centrifugal force around the wing is presented.

2. Governing equations

The governing equations for the current work are the compressible, three-dimensional Navier–Stokes equations. After a general time-dependent transformation from Cartesian coordinates (x, y, z, t) to computational space (ξ, η, ζ, τ), these equations can be written in strong conservation form (Tannehill, Anderson & Pletcher 1997) as follows:

$$\frac{\partial}{\partial \tau}\left(\frac{\boldsymbol{U}}{J}\right)+\frac{\partial \boldsymbol{F}}{\partial \xi}+\frac{\partial \boldsymbol{G}}{\partial \eta}+\frac{\partial \boldsymbol{H}}{\partial \zeta}=\frac{1}{Re}\left[\frac{\partial \boldsymbol{F}_v}{\partial \xi}+\frac{\partial \boldsymbol{G}_v}{\partial \eta}+\frac{\partial \boldsymbol{H}_v}{\partial \zeta}\right] \tag{2.1}$$

where the solution vector is

$$\boldsymbol{U}=[\rho,\ \rho u,\ \rho v,\ \rho w,\ \rho e]^{\mathrm{T}} \tag{2.2}$$

and the inviscid flux vectors are

$$\boldsymbol{F}=\frac{1}{J}\begin{bmatrix}\rho U\\ \rho uU+\xi_x p\\ \rho vU+\xi_y p\\ \rho wU+\xi_z p\\ (\rho e+p)\,U-\xi_t p\end{bmatrix},\quad \boldsymbol{G}=\frac{1}{J}\begin{bmatrix}\rho V\\ \rho uV+\eta_x p\\ \rho vV+\eta_y p\\ \rho wV+\eta_z p\\ (\rho e+p)\,V-\eta_t p\end{bmatrix},$$
$$\boldsymbol{H}=\frac{1}{J}\begin{bmatrix}\rho W\\ \rho uW+\zeta_x p\\ \rho vW+\zeta_y p\\ \rho wW+\zeta_z p\\ (\rho e+p)\,W-\zeta_t p\end{bmatrix}. \tag{2.3}$$

In these expressions, $J=\partial(\xi,\ \eta,\ \zeta,\ \tau)/\partial(x,\ y,\ z,\ t)$ is the Jacobian of the transformation, u, v and w are the Cartesian velocity components, ρ is the density, p is the pressure, U, V and W are the contravariant velocities given as

$$\left.\begin{aligned}U&=\xi_t+\xi_x u+\xi_y v+\xi_z w\\ V&=\eta_t+\eta_x u+\eta_y v+\eta_z w\\ W&=\zeta_t+\zeta_x u+\zeta_y v+\zeta_z w\end{aligned}\right\} \tag{2.4}$$

and the internal energy, e, is

$$e=\frac{T}{\gamma\,(\gamma-1)\,M_{ref}^2}+\tfrac{1}{2}\left(u^2+v^2+w^2\right) \tag{2.5}$$

where T is the temperature, γ is the ratio of specific heats, and M_{ref} is the reference Mach number. For the sake of brevity, the viscous fluxes, $\boldsymbol{F}_v$, $\boldsymbol{G}_v$ and $\boldsymbol{H}_v$, are not shown, but they are provided by Tannehill *et al.* (1997), for instance. The governing equations are also supplemented with the perfect gas equation, $p=\rho T/\gamma M_{ref}^2$, Sutherland's viscosity law, a constant Prandtl number ($Pr=0.72$ for air), and Stokes' hypothesis for the bulk viscosity coefficient ($\lambda=-2/3\mu$). For simulations of moving

https://doi.org/10.1017/jfm.2014.212 Published online by Cambridge University Press

wings in quiescent fluid, all velocity components are non-dimensionalized by the maximum speed, U_{ref}, of the body at some reference location along the wing, all length scales are scaled by the chord, and pressure is normalized by $\rho_{ref}U_{ref}^2$.

This set of equations corresponds to the unfiltered Navier–Stokes equations and is used without change in laminar, transitional or fully turbulent regions of the flow for the ILES procedure. Unlike the standard LES approach, no additional subgrid-scale (SGS) model or heat flux terms are appended. Instead, a high-order, low-pass filter operator, which will be discussed later, is applied to the conserved variables during the solution of the standard Navier–Stokes equations. This highly discriminating, Padé-type filter selectively damps only the high-frequency components of the solution, that are often times under-resolved by the mesh (Visbal & Rizzetta 2002). The filtering regularization procedure provides an attractive alternative to the use of standard SGS models, and has been found to yield suitable results for several turbulent and transitional flows on LES level grids (Garmann, Visbal & Orkwis 2013*a*). A reinterpretation of this ILES approach in the context of an approximate deconvolution model (Stolz & Adams 1999) has been provided by Matthew *et al.* (2003). For the present low-Reynolds-number flows, the ILES approach is effectively a direct numerical simulation (DNS).

3. Numerical procedure

All simulations are performed with the extensively validated high-order, Navier–Stokes solver, FDL3DI (Gaitonde & Visbal 1998; Visbal & Gaitonde 1999). In this code, a finite-difference approach is employed to discretize the governing equations, and all spatial derivatives are obtained with high-order compact-differencing schemes (Lele 1992). At boundary points, higher-order one-sided formulas are utilized that retain the tridiagonal form of the scheme (Gaitonde & Visbal 1998; Visbal & Gaitonde 1999). The derivatives of the inviscid fluxes are obtained by forming the fluxes at the nodes and differentiating each component with the compact differencing scheme. Viscous terms are obtained by first computing the derivatives of the primitive variables. The components of the viscous fluxes are then constructed at each node and differentiated by a second application of the same scheme.

In order to eliminate spurious components of the solution, a high-order, low-pass spatial filtering technique (Gaitonde & Visbal 1999; Visbal & Gaitonde 1999) is incorporated that is based on templates proposed by Alpert (1981) and Lele (1992). With proper choice of coefficients, it provides a $2N$th-order formula on a $2N + 1$ point stencil. These coefficients, along with representative filter transfer functions, are provided by Gaitonde & Visbal (1998) and Gaitonde & Visbal (1999). The filter is applied to the conserved variables along each transformed coordinate direction one time after each time step or subiteration. For the near-boundary points, the filtering strategies described by Gaitonde & Visbal (1999) and Visbal & Gaitonde (1999) are used. For transitional and turbulent flows, the high-fidelity spatial algorithmic components provide an effective ILES approach in lieu of traditional SGS models, as demonstrated by Visbal & Rizzetta (2002) and Visbal, Morgan & Rizzetta (2003) and more recently by Garmann *et al.* (2013*a*). All computations presented here are performed with a sixth-order interior discretization scheme coupled with an eighth-order accurate implicit filter.

Time marching of the governing equations is achieved through the iterative, implicit approximately factored integration method of Beam & Warming (1978). This method has been simplified through the diagonalization of Pulliam & Chaussee (1981) and

https://doi.org/10.1017/jfm.2014.212 Published online by Cambridge University Press

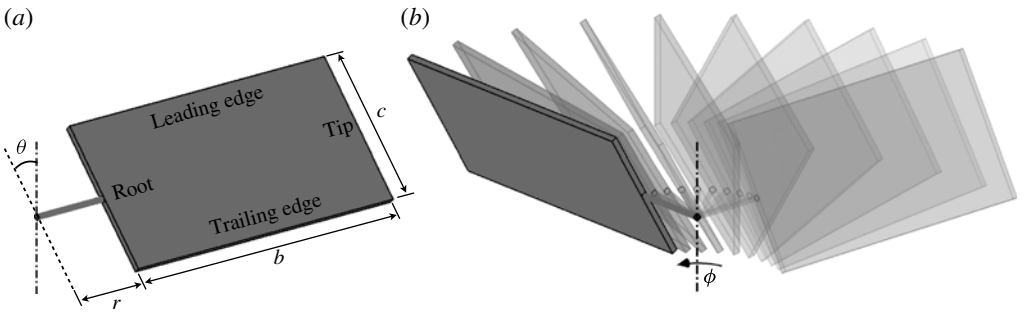


FIGURE 1. Geometry definition and revolving configuration: (*a*) wing geometry; (*b*) revolving orientation.

supplemented with the use of Newton-like subiterations to achieve second-order accuracy (Visbal & Rizzetta 2002; Visbal *et al.* 2003). Subiterations are commonly used to reduce errors due to factorization, linearization, diagonalization and explicit specification of boundary conditions (Rizzetta, Visbal & Morgan 2008). Fourth-order, nonlinear dissipation terms (Jameson, Schmidt & Turkel 1981; Pulliam 1986) are also appended to the implicit operator to augment stability.

For all revolving wing simulations presented in this work, the entire mesh is moved in a rigid fashion using the prescribed kinematics. The time-metric terms are evaluated employing the procedures described in detail by Visbal & Gaitonde (2002) to ensure that the geometric conservation law (GCL) is satisfied.

4. Details of the computations

4.1. *Geometry and kinematic definitions*

Three rectangular wings are considered for this study with $AR = 1$, 2 and 4, respectively. Each wing also features a rectangular cross-section with a thickness of $0.041c$ following the experiments considered by Ozen & Rockwell (2012*a*). The root of each wing is extended out a distance of $r_{root} = 0.5c$ from the axis of rotation with the chord oriented at an angle of $\theta = 30°$ relative to the axis as depicted in figure 1(*a*). The wings start from rest and in quiescent fluid before accelerating to a constant rotational rate as they revolve as shown in figure 1(*b*). The angle of rotation during the motion, $\phi(\tau)$, is given by

$$\phi(\tau) = \frac{\dot{\phi}^*_{max}}{2a} \ln\left[\frac{\cosh(a(\tau - \tau_1))}{\cosh(a(\tau - \tau_2))}\right] + \tfrac{1}{2}\phi_0 \tag{4.1}$$

where the dimensionless time is $\tau = t\,U_{ref}/c$, the maximum angle of rotation is ϕ_0 and $\dot{\phi}^*_{max} = \dot{\phi}_{max}c/U_{ref}$ is the normalized rotational rate. The parameter, a, controls the smoothness of the function with smaller values reducing the maximum angular acceleration and causing a smoother motion profile. If no smoothing were present, τ_1 is the time until the sharp start-up of the unsmoothed motion, and τ_2 is the end time of the motion, $\tau_2 = \tau_1 + \phi_0/\dot{\phi}^*_{max}$ as shown in figure 2. Equation (4.1) is a modified form of a function described by Eldredge, Wang & Ol (2009) which allows for a continuous motion that is sufficiently differentiable, thereby avoiding discontinuities

https://doi.org/10.1017/jfm.2014.212 Published online by Cambridge University Press

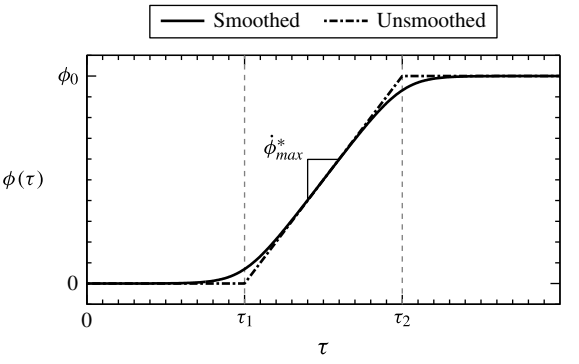


FIGURE 2. Rotational angle in time.

in the angular acceleration. This simple, unidirectional revolving motion provides a means of examining, for example, a single stroke of hovering or a take-off motion for a biological flier.

Since the wing rotates in quiescent fluid (i.e. no free-stream velocity), some other reference speed must be chosen for normalization. This speed is selected as the maximum rotational velocity achieved at the wing root ($U_{root} = r_{ref}\dot{\phi}_{max}$) in order to provide a consistent variation of the local span-based Reynolds number for each wing. The $AR = 2$ and 4 wings then operate as if they are simply extensions of the $AR = 1$ wing. Normalization in this manner leads to a dimensionless rotational rate given as

$$\dot{\phi}^*_{max} = \frac{\dot{\phi}_{max} c}{U_{root}} = \frac{\dot{\phi}_{max} c}{(r_{root}\dot{\phi}_{max})} = \frac{c}{r_{root}} = 2.0 \tag{4.2}$$

which is a purely geometric quantity driven solely by the normalized root radius of the wing, $(r_{root}/c) = 0.5$. Further, all simulations presented in this work rotate a complete revolution, $\phi_0 = 2\pi$, and utilize a smoothing parameter of $a = 5.2$. The start time is set as $\tau_1 = 0.75$ leading to $\tau_2 = 3.89$, and the time step for all computations is selected as $\Delta\tau = 5.0 \times 10^{-5}$.

4.2. *Computational mesh and boundary conditions*

In order to discretize the domain around the rectangular wings, six structured grids were constructed off the root, tip, upper, lower, leading- and trailing-edge surfaces that each maintain sufficient near-body and wake resolution before stretching to the farfield. A generic depiction of the multiblock nearfield domain used in this study can be seen in figure 3. Note that each block actually extends outward to at least 30 chords from the body using 81 points with increased stretching near the farfield boundary. Only the nearfield is depicted in figure 3 for clarity. The wing surface is discretized with 131 points distributed across the chord (ξ direction) and 41 points across the thickness (η direction). The number of spanwise points (ζ direction) scales with aspect ratio: 131, 261 or 521 points are used for $AR = 1$, 2 or 4, respectively. The initial off-body spacing and corner surface spacing is $\Delta n_i = 0.0005$ chords. Grid clustering immediately off the body and around the wing edges is maintained throughout the domain. The resulting sizes of each block ($n_\xi \times n_\eta \times n_\zeta$) are listed in table 1 for each aspect-ratio wing.

https://doi.org/10.1017/jfm.2014.212 Published online by Cambridge University Press

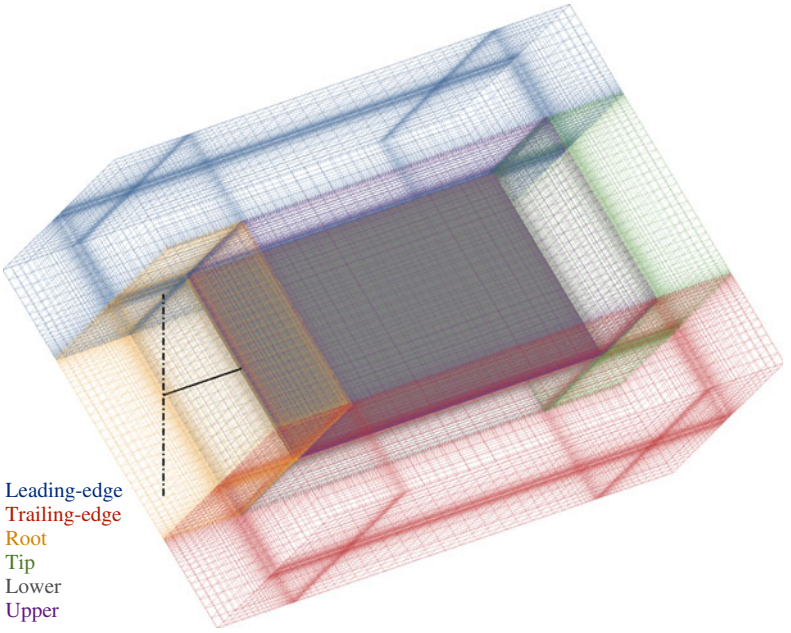


FIGURE 3. Nearfield computational mesh. Note that the farfield boundaries actually extend to a distance of 30 chords from the wing, but only the nearfield is shown for clarity.

The upper and lower surface meshes extend four grid planes into the leading- and trailing-edge blocks and into the root and tip sections to provide point-to-point communication between the adjacent blocks. The root and tip blocks similarly extend into the leading- and trailing-edge sections. Note that these extended planes of data are overwritten each subiteration with the values obtained from the interior of the adjacent block. In the case of the maneuvering wing, the entire domain rotates at the prescribed motion with varying kinematics.

The boundary condition on the wing surface is specified as a no-slip, adiabatic moving wall with zero-normal pressure gradient approximated by a fourth-order accurate extrapolation. The farfield boundary in each block, which is located 30 chords from the wing surface, is set as a zero-velocity condition with the reference temperature and density each as unity. Near this boundary, each mesh is stretched

				$AR=1$		$AR=2$		$AR=4$
Block	n_ξ	n_η	n_ζ	Points	n_ζ	Points	n_ζ	Points
Leading edge	81	201	291	4 737 771	421	6 854 301	681	11 087 361
Trailing edge	81	201	291	4 737 771	421	6 854 301	681	11 087 361
Root	137	201	81	2 230 497	81	2 230 497	81	2 230 497
Tip	137	201	81	2 230 497	81	2 230 497	81	2 230 497
Lower surface	137	81	137	1 520 289	267	2 962 899	527	5 848 119
Upper surface	137	81	137	1 520 289	267	2 962 899	527	5 848 119
				16 977 114		24 095 394		38 331 954

TABLE 1. Computational mesh sizes for the various aspect-ratio wings.

https://doi.org/10.1017/jfm.2014.212 Published online by Cambridge University Press

AR	Re_{root}	Re_{r_g}	Re_{tip}
1	1000	2000	3000
2	1000	3000	5000
4	1000	5000	9000

TABLE 2. Reynolds numbers based on the maximum root, midspan and tip speeds.

quite rapidly, which, in conjunction with the low-pass filter, provides a buffer-type treatment of the boundary that eliminates spurious reflections associated with the imposed flow condition. The reference Mach number for all computations is selected as $M_{ref} = 0.1$ to minimize effects of compressibility.

The revolving, $AR = 1$ wing was simulated with the mesh described above along with two other meshes of successive spatial resolution by Garmann *et al.* (2013*b*). The Reynolds number for those simulations was $Re_{root} = 7250$, which is much higher than the values used in the current study. This grid was found to provide sufficient spatial resolution of the three-dimensional flow structure when compared with the other resolutions, and the unsteady aerodynamic loads that were produced throughout the motion also showed only slight sensitivity to spatial resolution. In addition, comparisons of the baseline mesh solution with experimental particle image velocimetry (PIV) measurements from Ozen & Rockwell (2012*a*) showed remarkably favourable agreement throughout the motion. The refinement study and experimental comparisons by Garmann *et al.* (2013*b*) provide a high level of confidence in the choice of resolutions for the meshes used in the current study.

5. Results

The effects of aspect ratio on the three-dimensional flow structure and aerodynamic loads are examined in this section. Three wings are considered with $AR = 1$, 2 and 4, respectively. The Reynolds number based on the maximum rotational velocity achieved at the *root* is selected as $Re_{root} = 1000$ for all cases. This allows the variation of Reynolds number along the span to remain consistent for all aspect ratios considered, which means that the higher-aspect-ratio wings operate as if they are extensions of the aspect-ratio-one wing. The corresponding midspan and tip Reynolds numbers for the different aspect ratios are listed in table 2 for reference.

5.1. *Description of unsteady flow structure*

The three-dimensional flow structure is shown in figure 4 for rotational angles $\phi = 15$, 45, 90 and 135°through iso-surfaces of relative total pressure. Two surfaces are shown to highlight the inner core and outer shell of the vortex system. Representation of the solution through the total pressure has been shown previously to provide a clear interpretation of the overall flow structure by masking many of the smaller scales associated with transition and vortex breakdown while preserving the coherence of the vortex core (Garmann *et al.* 2013*b*).

Shortly after the onset of the motion at $\phi = 15°$, distinct vortices can be seen emanating from the edges of the wing that are anchored to their respective corners. By $\phi = 45°$, the leading-edge, tip and trailing-edge vortices have unpinned from the outboard corners of the wing and undergo a reconnection process to form a continuous vortex loop that increases size with aspect ratio since the travel distance at the tip

https://doi.org/10.1017/jfm.2014.212 Published online by Cambridge University Press

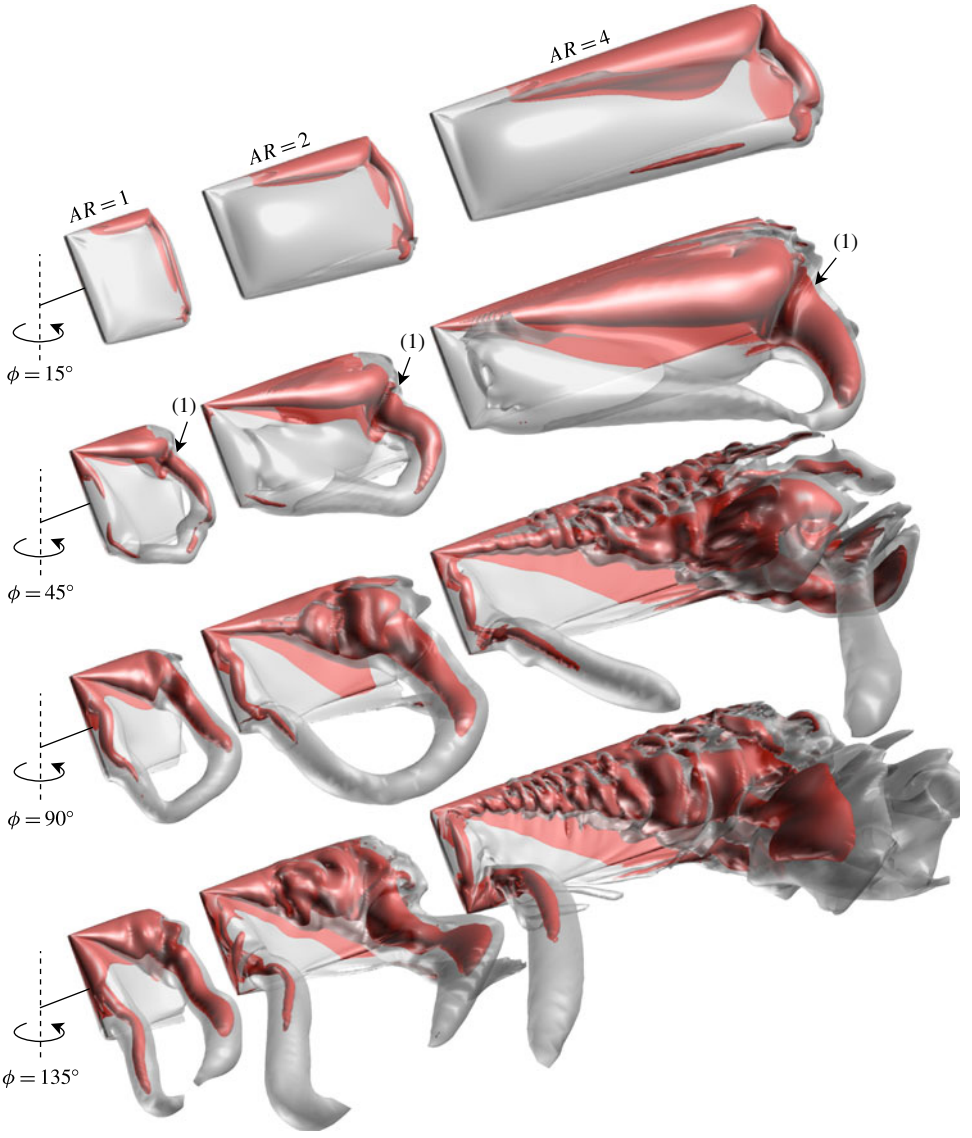


FIGURE 4. Dual isosurfaces of relative total pressure showing the three-dimensional vortex structure about the revolving wings. Here (1) denotes the reconnection of the leading-edge and tip vortices.

also scales with span. The initial pinning allows the middle sections of leading edge and tip vortices to progress aft while keeping the end sections anchored, producing an arch-like LEV. It should be noted that this initial arch-like lift-off has been observed experimentally by Ozen & Rockwell (2012*b*) and Carr *et al.* (2013). When the ends finally unpin from the front corner and connect, the arch-like shape of either vortex is maintained resulting in a slight kink at the connection point, which is denoted as (1) in the figure. Later in the motion, the LEV lifts off slightly form the outboard section of the wing as it reorients along the tip and the kink relaxes and opens to a loop

https://doi.org/10.1017/jfm.2014.212 Published online by Cambridge University Press

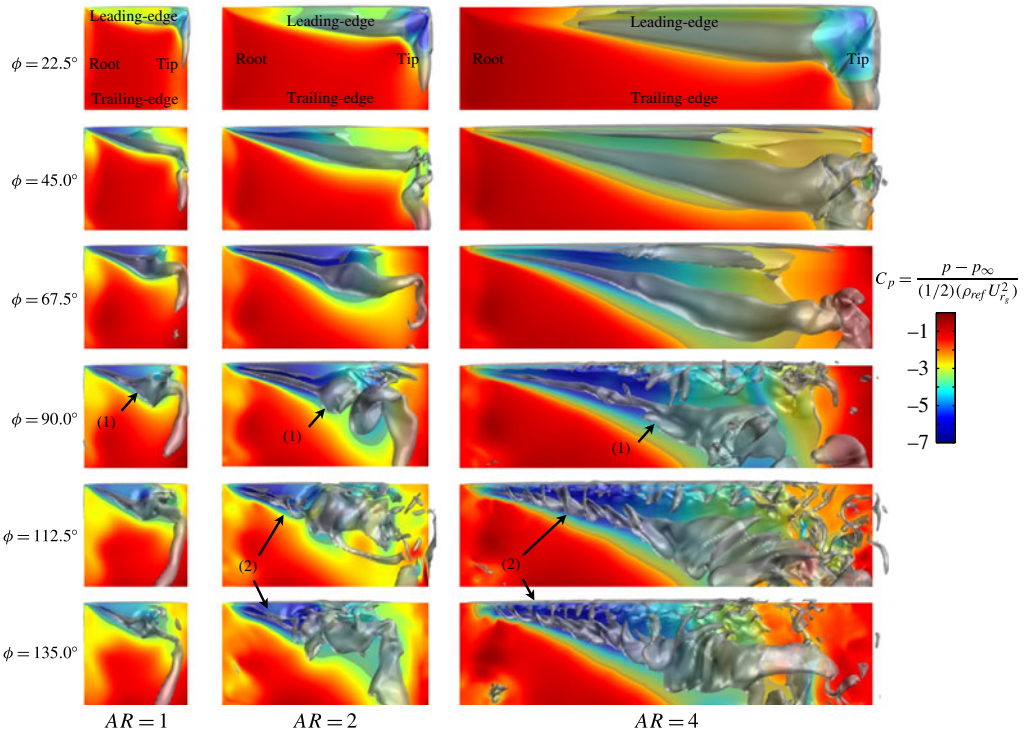


FIGURE 5. Evolution of the surface pressure distribution on the suction side of the wing with overlaid isosurface of relative total pressure highlighting the vortex core along the leading edge. Here (1) denotes the expansion of the vortex core due to breakdown and (2) indicates the undulation of the vortex core for higher aspect ratios.

structure that connects the leading edge, tip, trailing edge and root vortices. Although the tip/trailing edge portion of the structure appears disconnected with the chosen value of total pressure in figure 4, it is, indeed, connected. The size of the vortex loop increases with aspect ratio since the travel distance at the wingtip also scales with span, but the overall development of the vortex system is similar for each aspect ratio. It is also worth noting the good qualitative agreement of many of these features with the computational results of Harbig *et al.* (2013) for a completely different planform of a fruit fly wing, which highlights the robustness of these flows.

A more detailed evolution of each vortex core for $22.5° \leqslant \phi \leqslant 135°$ can be seen in figure 5 through another isosurface of relative total pressure and the surface pressure distribution on the suction side of the wing. Note that the pressure coefficient is renormalized by the maximum midspan velocity, $U_{r_g}^2$, rather than the root in order to more directly compare the different aspect ratios. The proximity of the vortex to the surface of the wing promotes a strong region of suction along the leading edge that persists to the midspan, regardless of aspect ratio. Past midspan, the vortex lifts off the surface into an arch-type structure as it reorients itself along the tip, which diminishes its imprint in the surface pressure and reduces the suction near the tip. At $\phi = 90°$, the inboard pressure is largely established for all aspect ratios. At this same instant, an expansion of the vortex core is identifiable as a bubble-like structure for each wing around midspan (denoted as (1)), which is indicative of vortex breakdown.

https://doi.org/10.1017/jfm.2014.212 Published online by Cambridge University Press

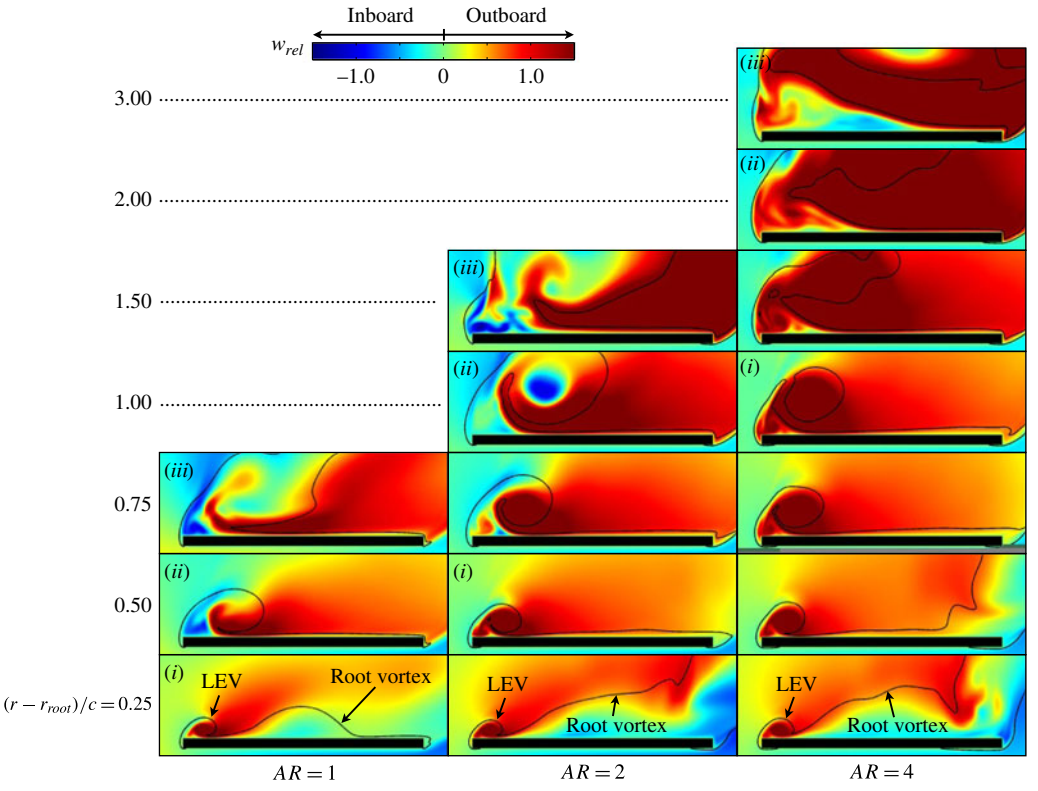


FIGURE 6. Contours of relative spanwise velocity at $\phi = 90°$ along with a single contour line of relative total pressure ($p_0/p_{0,ref} = 0.99$) to highlight the LEV. View is directed from root to tip, and all components are normalized by the maximum rotational velocity at the midspan. Images with (i), (ii) or (iii) correspond to span-normalized locations of 25, 50 and 75 %, respectively, for each wing.

Beyond the bubble in the spanwise direction, the LEV core exhibits a helical shape that winds opposite the sense of rotation of the vortex, which is consistent with a switch in sign of the azimuthal vorticity seen with vortex breakdown (Visbal 1994). At $\phi = 112.5$ and 135.0°, spiraling undulations of the vortex core (denoted as (2)) can be seen with the higher-aspect-ratio wings resulting from interactions with the wall. Also with the higher aspect ratios, the chordwise extent of the LEV reaches a point at which it occupies the entirety of the wing, and thereby hindering its continued growth along the span. Once this occurs, the LEV begins to entrain reversed-signed vorticity from the trailing edge that promotes outboard separation and a further loss of suction near the tip. The geometric constraint of the vortex growth and resulting pressure loss impacts the aerodynamic loading on the wing, which is discussed later.

Contours of the relative spanwise velocity at $\phi = 90°$ are shown in figure 6 at several spanwise stations. A single contour line of relative total pressure ($p_0/p_{0,ref} = 0.99$) is superimposed in each image as well to highlight the LEV, and the view is directed from root to tip. The velocity is normalized by the maximum speed achieved at the midspan of the wing during rotation, U_{r_g}. For each aspect ratio, a coherent LEV is visible from the root of the wing until the effects of the tip force the LEV to lift off and reorient in the chordwise direction. In addition, there are large regions of strong

https://doi.org/10.1017/jfm.2014.212 Published online by Cambridge University Press

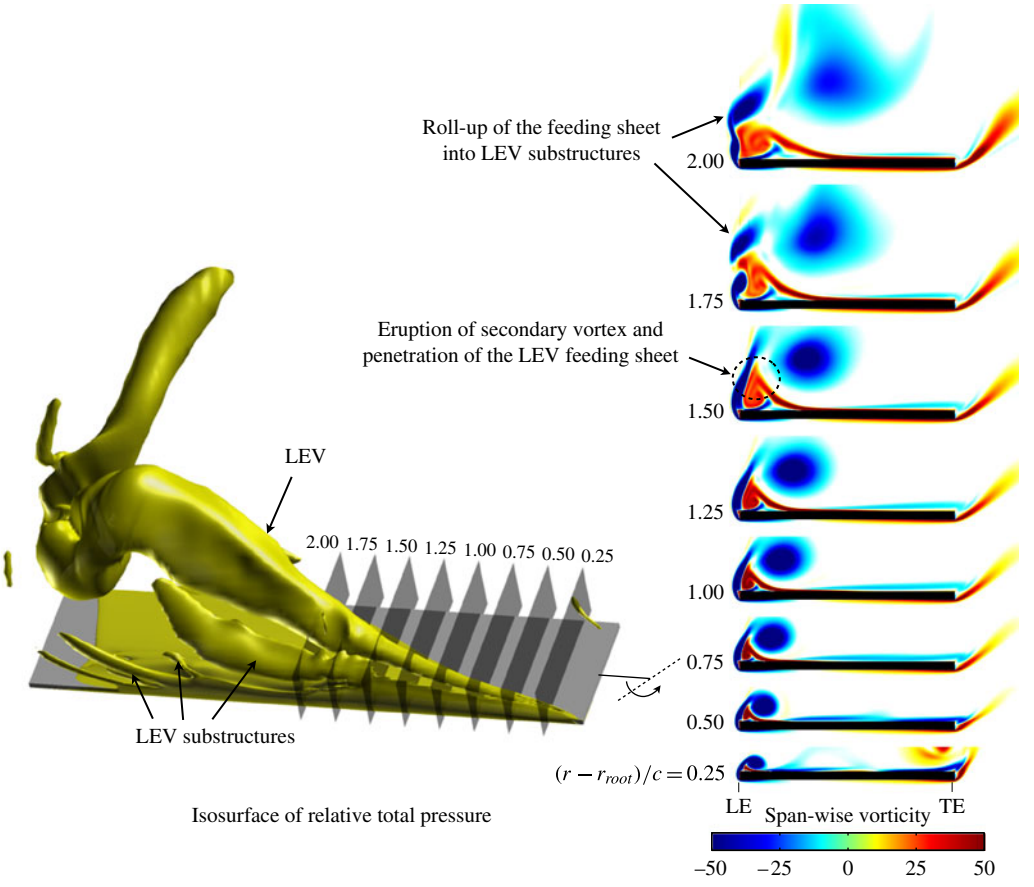


FIGURE 7. Evolution of the LEV along the span of the aspect-ratio-four wing. Solution corresponds to a rotational angle $\phi = 67.5°$.

outboard flow present past the LEV in the chordwise direction regardless of aspect ratio. At a distance of 0.25 chords from the wing root, all solutions show a similarly sized LEV with a strong outboard jet present in its core that is of the order of the midspan rotational velocity. A portion of the root vortex is present in these images as well due to the proximity of the viewing plane to the wing root. At 0.50 chords from the root, the $AR = 1$ wing produces a relatively enlarged LEV from the proximity of the tip with a region of reversed flow present in its feeding sheet emanating from the leading edge. At the midspan for $AR = 2$ (1.0 chord from the root), an abrupt flow reversal is observed in the vortex core that corresponds to the bubble-like structure that was pointed out in figure 5 and is, again, consistent with breakdown. For all aspect ratios, the LEV is lifted-off the surface as it approaches the tip around the 75 % span location. Regions of reversed flow are also present underneath the LEV at these sections that allow transitional structures from the separated region near the wingtip to convect inboard slightly, leading to further complexity of the LEV feeding sheet.

The genesis and evolution of the LEV along the span of the aspect-ratio-four wing at $\phi = 67.5°$ is shown in figure 7 through contours of spanwise vorticity at several stations that dissect the LEV. An isosurface of total pressure is also shown to highlight the three-dimensionality of the vortex system at this instant. Close to the root of

https://doi.org/10.1017/jfm.2014.212 Published online by Cambridge University Press

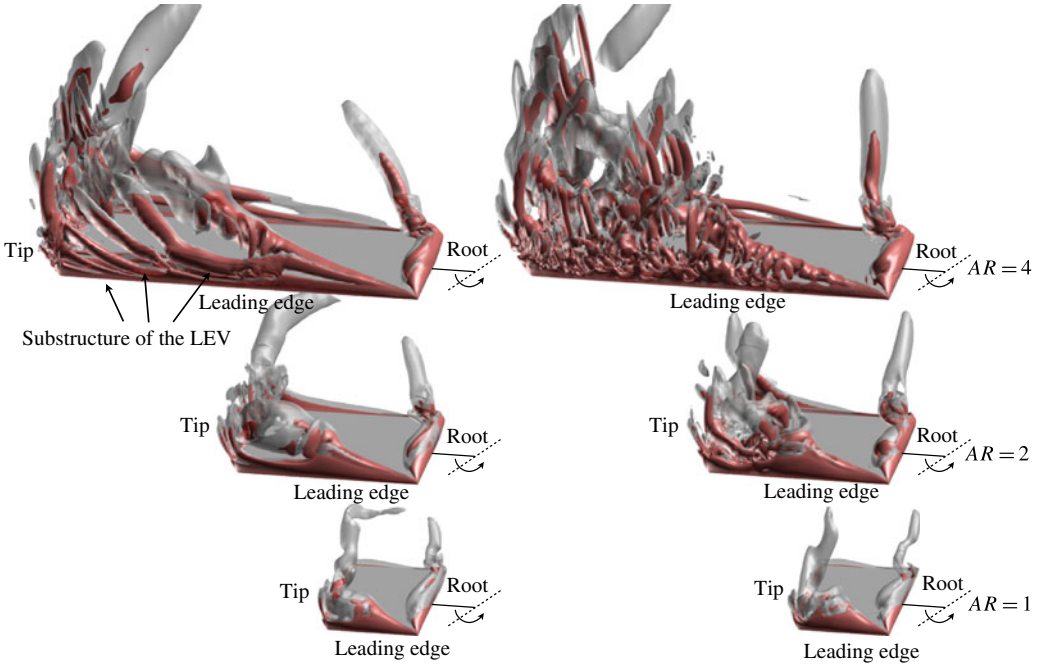


FIGURE 8. The Q-criterion isosurfaces showing the evolution of the LEV along the span for each aspect ratio. Solutions correspond to rotational angles $\phi = 67.5$ and $90.0°$.

the wing, the LEV appears as a tight and coherent vortex. A secondary vortex is formed from the induced vorticity generated between the LEV and the plate surface. The size of the LEV and secondary vortex continue to grow proportionally along the span until a distance of 1.5 chords from the wing root, where the secondary vortex erupts from the surface and penetrates the LEV feeding sheet. The disrupted shear layer rolls up under self-induction and forms substructures that rotate in the same direction as the LEV. These finger-like substructures are apparent off the leading edge in the spanwise vorticity and in the three-dimensional isosurface of total pressure at a distance greater than 1.75 chords from the root. Similar transitional elements have been seen both computationally and experimentally for a revolving wing by Carr *et al.* (2013) and Harbig *et al.* (2013), respectively; although, they are described as 'dual-LEVs'. Past $\phi = 67.5°$, the substructures present within the LEV feeding sheet for the $AR = 4$ wing become susceptible to instabilities and breakdown into much smaller scales resulting in a more complex flow structure near the tip. This is shown in the Q-criterion isosurfaces of figure 8. The wings with $AR = 1$ and 2 are also shown for comparison. Discrete vortices have also been observed shedding from the trailing edge, but these features are quickly entrained into the vortex loop or dispersed in the outboard separated region and lose their coherence very quickly. The lower-aspect-ratio wings in this study do not show the same substructure development within the LEV feeding sheet, indicating that their formation is a result of the local span-based Reynolds number achieved during rotation. The wings with $AR \leqslant 2$ do not have sufficient span for these features to manifest before the flow is overcome by the influence of the tip. However, as reported by Garmann *et al.* (2013*b*), increasing Reynolds number for a fixed aspect ratio leads to the formation of these substructures.

https://doi.org/10.1017/jfm.2014.212 Published online by Cambridge University Press

It is important to note that the inception and evolution of the LEV substructure that was detailed above very closely resembles the mechanisms described by Gordnier & Visbal (1993) and Visbal & Gordnier (2003) for the formation of shear-layer structures within the LEV formed on swept delta wings. In those studies, the development of the shear-layer structure was shown to be dependent upon the local, length-based Reynolds number measured from the apex of the wing. Alternatively, vortex breakdown was shown to be a result of the pressure gradient established between the wing apex and the trailing edge (Visbal 1994) and independent of the length-based Reynolds number. Likewise, the formation of LEV substructures for a revolving wing seems to correlate with the local, span-based Reynolds number, while breakdown appears to be more dependent on the pressure gradient established between the root and tip of the wing (see, for example, Maxworthy 2007) since breakdown was shown to occur near midspan regardless of aspect ratio. Perhaps the close resemblance can be explained by the coupled spanwise and rotational velocities present with a revolving wing that bias the flow direction outboard and act almost as the convective velocity over a delta wing. Regardless, these parallels between revolving wings and swept delta wings may be extremely important for the continued understanding of flapping wing dynamics.

5.2. *Aerodynamic loads*

The lift, drag and pitching moment coefficients are shown in figure 9(*a*). It is important to note that these coefficients have been renormalized by the midspan velocity, U_{r_g}, for comparison and use the wetted area of the chord times the span, $S = c\,b$. Relative to the other components, the radial forces are insignificant throughout the motion for each aspect ratio, so they are not shown. In all cases, the attached LEV provides substantial and sustained loading throughout the motion. At the onset of the motion, the lift, drag and pitching moment coefficients increase very quickly due to the angular acceleration of the plate. Shortly thereafter, the coefficients plateau and then increase at a much lower rate as the vortex system strengthens and grows. By $\phi = 90$, where the inboard surface pressure was seen to be largely established, the force and moment coefficients from the higher-aspect-ratio wings mostly level off and exhibit unsteady fluctuations around nearly the same mean value. At this point in the motion, the chordwise extent of the LEV for the higher-aspect-ratio wings has grown to a size that covers the entire chord as observed from the pressure distributions of figure 5. The growth of the LEV becomes constrained by the trailing edge, which causes the forces and moment to saturate. For $AR = 1$, the extent of the LEV never encompasses the entire chord of the wing, so its development is unhindered by the trailing edge, allowing the coefficients to increase gradually during the motion; however, they never quite reach the higher peak values achieved by the other aspect ratios. The persistent pitch-up radial moment in the latter part of the motion is a sign that the chordwise aerodynamic centre remains mostly stationary once the flow is established.

The sectional lift coefficient, $c_l' = L'/(1/2\rho_{ref} U_{r_g}^2 c)$, plotted against the normalized spanwise location is shown in figure 9(*b*) for rotational angles $\phi = 45$, 90, 135 and 270°. Early in the motion, at $\phi = 45°$, a sectional lift peak is present near the wingtip from the relatively close proximity of the tip vortex to the surface. As the wing progresses further, however, the tip vortex separates and lifts away from each wing, causing its contribution to the sectional lift to diminish. Throughout their motions, the two lower-aspect-ratio wings produce lift distributions that predominantly increase

https://doi.org/10.1017/jfm.2014.212 Published online by Cambridge University Press

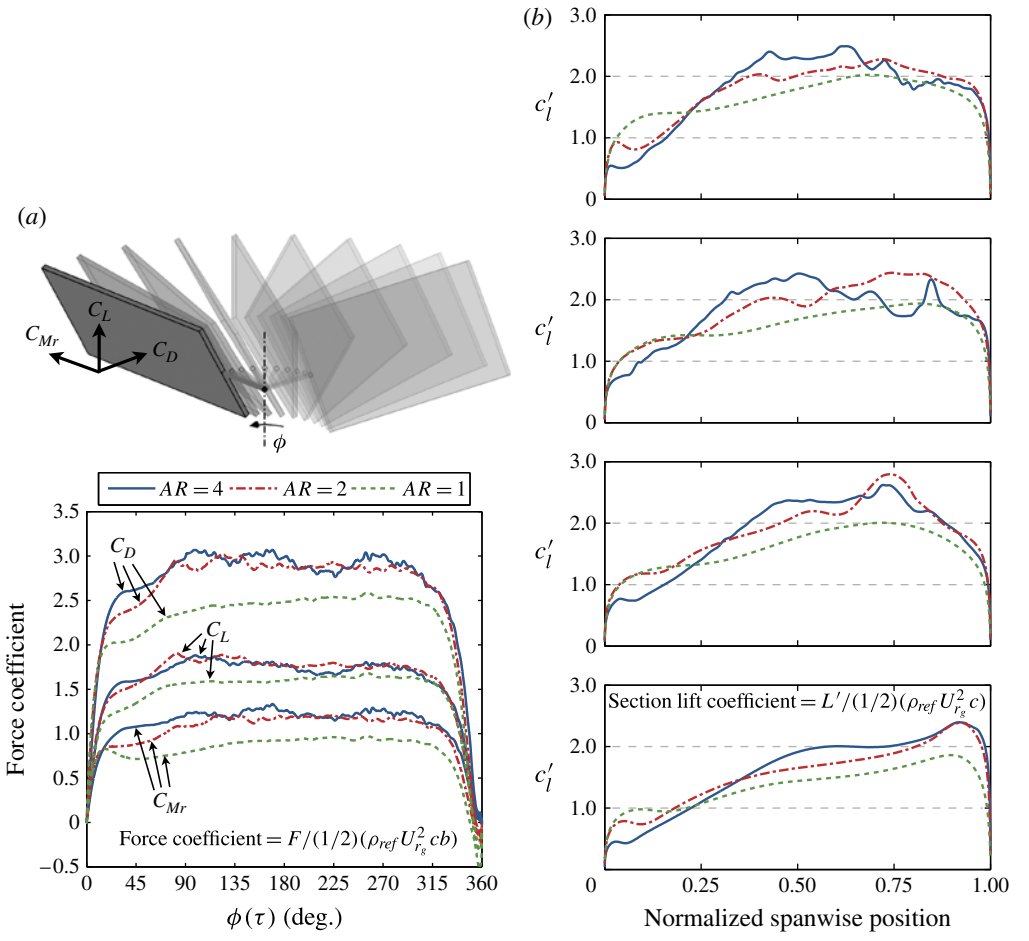


FIGURE 9. Lift, drag and pitching moment coefficients and the sectional lift coefficient across the span for at rotational angles $\phi = 45$, 90, 135 and 270°: (*a*) instantaneous aerodynamic loads; (*b*) spanwise sectional lift distributions.

across the majority of their spans until just before the wing tip where the LEV has lifted away from the surface. For $AR = 4$, the initial distributions at $\phi \leqslant 90°$ behave similarly; however, later in the motion, there is a loss of sectional lift outboard of midspan as a result of the constrained LEV growth and outboard separation.

There are a number of very important points that should be emphasized here. First, with sufficient span, there exists a geometric constraint on the growth of the LEV by the trailing edge that results in a saturation of the aerodynamic loads. Thus, for the kinematics and geometry examined here, there is no advantage of increasing aspect ratio once the extent of the LEV occupies the entire chord of the wing, which occurs near $AR = 2$. For lower-aspect-ratio wings, where the extent of the LEV never reaches the trailing edge, the instantaneous loads continue to increase gradually throughout the wing's revolution. This is seen for the $AR = 1$ wing in figure 9(*a*), and similar behaviour has been shown over a broad range of Reynolds numbers in a previous study (Garmann *et al.* 2013*b*). Next, the LEV substructures formed around the $AR = 4$ wing due to the high local, span-based Reynolds number do not seem to

https://doi.org/10.1017/jfm.2014.212 Published online by Cambridge University Press

impact overall force production, but may lead to slightly higher unsteady fluctuations around the mean loading indicated by the larger oscillations of the drag coefficient in figure 9(*a*) for the $AR = 4$ wing when compared with the other wings. Finally, as was shown by Birch *et al.* (2004) and others, increased Reynolds number can also provide benefits in force production with eventual saturation; however, based on the flow structure and pressure distributions discussed previously, the saturation observed in figure 9(*a*) appears to be a direct consequence of the geometric constraint mentioned above.

5.3. *Separation of dynamic forces for the revolving wing*

When the non-dimensionalized Navier–Stokes equations are cast into a rotating frame of reference, the apparent angular, centrifugal and Coriolis forces appear on the right-hand side of the equations as source terms. These forces, when summed with the pressure gradient force and neglecting the viscous forces, form the total dynamic force seen by the fluid measured in the moving reference frame. This force is formulated as follows:

$$\boldsymbol{F}_{dyn} = -\nabla p \underbrace{-\rho\,\dot{\boldsymbol{\Omega}} \times \boldsymbol{r}}_{\boldsymbol{F}_{ang}} \underbrace{-\rho\,\boldsymbol{\Omega} \times (\boldsymbol{\Omega} \times \boldsymbol{r})}_{\boldsymbol{F}_{cen}} \underbrace{-2\rho\,(\boldsymbol{\Omega} \times \boldsymbol{u})}_{\boldsymbol{F}_{Cor}} \tag{5.1}$$

where $\boldsymbol{r}$ is the radius from the rotational axis, $\boldsymbol{u} = \boldsymbol{V} - (\boldsymbol{\Omega} \times \boldsymbol{r})$ is the relative velocity, and $\boldsymbol{\Omega}$ is the rotational rate of the system. The angular, centrifugal and Coriolis forces are designated as $\boldsymbol{F}_{ang}$, $\boldsymbol{F}_{cen}$ and $\boldsymbol{F}_{Cor}$, respectively. The Rossby number, which appears in some non-dimensionalizations of rotational forces, does not appear in this normalization since the dimensional form of $\boldsymbol{\Omega}$ is normalized by U_{ref}/c, and the radius, r, is normalized by the chord.

The total dynamic force is decomposed into its centrifugal, Coriolis and pressure gradient contributions. The spanwise components of these forces are shown in figure 10 at the 25 % span location for each aspect ratio at a rotational angle $\phi = 90°$. The forces are normalized by the midspan velocity, $U_{r_g}^2$. For each wing, the centrifugal force is consistently directed outboard and of the order of unity, but scales with distance from the rotational axis. The component of Coriolis force operates mostly on the edges of the LEV with an outboard contribution on the rearward side, and an inboard contribution on the forward and upper edge. It is also of the order of unity but has a diminishing magnitude with aspect ratio. The pressure gradient force acts in a dipole-like distribution that is an order of magnitude greater than the other two forces in the spanwise direction. A large region of outboard forcing encompasses the rear and upper portions of the LEV that prevails to the wing surface. A smaller region of inboard forcing is present in the forward section of the LEV core. This force is responsible for the deceleration and eventual flow reversal of the coherent jet in the vortex core. The spanwise total dynamic force is quite obviously dominated by the pressure gradient; however, there is a low, but consistent, outboard contribution from the centrifugal force. These two components are responsible for the outboard flow that was shown in figure 6 around almost the entirety of the suction side of the wing.

Next, the surface-normal component of the total dynamic force and its decomposed forces are shown in figure 11 at the 25 % span locations of each wing. On a spanwise plane, the centrifugal force in the normal direction is negligible in these regions since it is a radially directed force, so it is not shown. The Coriolis force exhibits moderate contributions in the normal direction with an upward-directed force in the core and

https://doi.org/10.1017/jfm.2014.212 Published online by Cambridge University Press

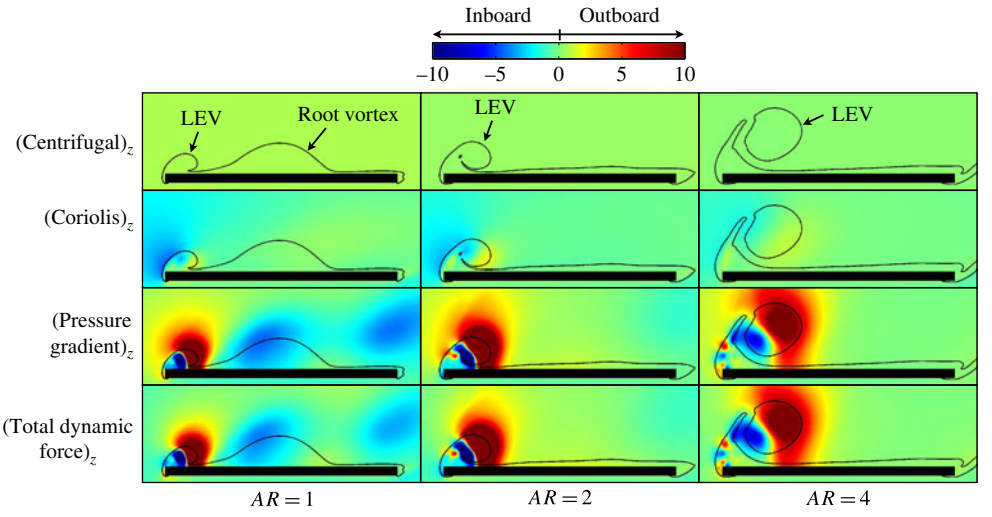


FIGURE 10. Contours of the spanwise components of the centrifugal, Coriolis, pressure gradient and total dynamic forces at the 25 % span location and $\phi = 90°$.

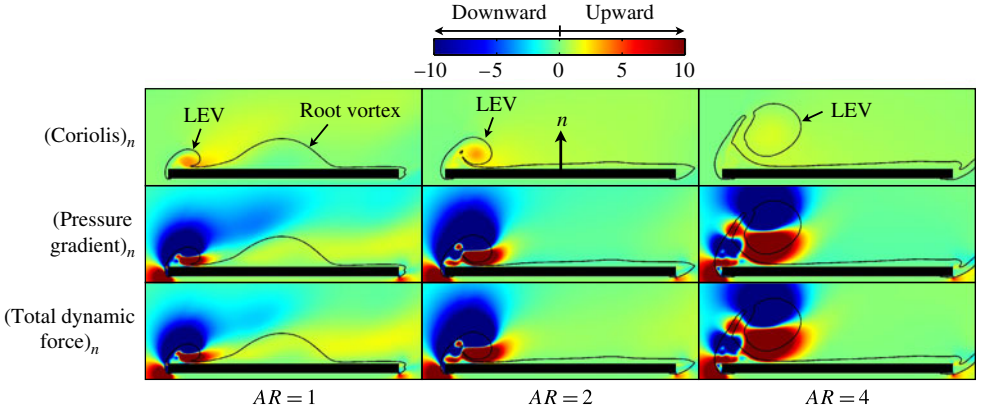


FIGURE 11. Contours of the surface-normal components of the Coriolis, pressure gradient and total dynamic forces at the 25 % span location and $\phi = 90°$.

at the base of the LEV. The upward direction demonstrates that Coriolis does not contribute to LEV attachment, but rather, quite the opposite. This same finding was provided by Garmann *et al.* (2013*b*) for an aspect-ratio-one wing over a broad range of Reynolds numbers; however, it was unclear whether that was merely an effect of increased interactions due to the close proximity of the wingtip. The findings presented in this work clearly show that even with reduced tip effects as the span is increased, Coriolis force still shows the same trends. The pressure gradient force is directed towards the vortex centre, which is expected from local rotation of the vortex core. This force is, again, shown to dominate the two forces by an order of magnitude and is almost indistinguishable from the total dynamic force.

The spanwise and surface-normal components of the forces are integrated across a sectional area at each spanwise location along the wing in order to quantify each forces' net contribution. The area selected extends from the wing surface to a normal

https://doi.org/10.1017/jfm.2014.212 Published online by Cambridge University Press

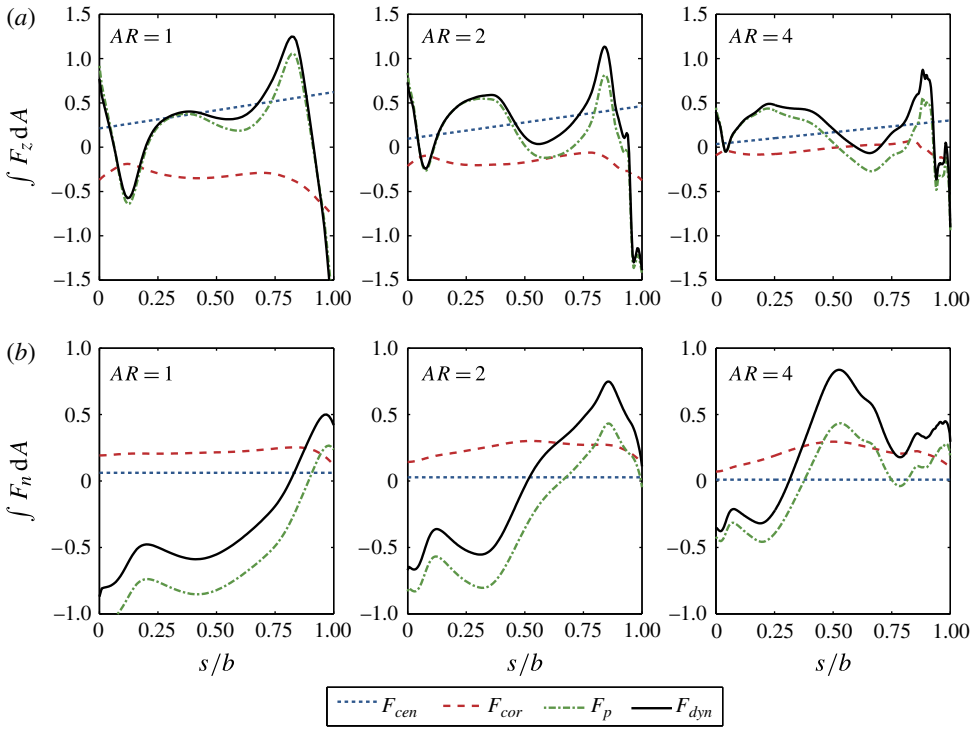


FIGURE 12. Net contributions of (*a*) the spanwise and (*b*) the surface-normal forces across the span at $\phi = 90°$. At each spanwise location, the force components are integrated across an area that extends from the wing surface to half a chord off the suction side and 0.1 chords off the leading and trailing edges.

distance of half a chord and also from $0.1c$ ahead of the leading edge to $0.1c$ behind the trailing edge. Figure 12 shows the integrated values at each spanwise location for all of the forces discussed above. Each component is plotted against the span-normalized distance from the wing root.

A strong similarity is seen between the integrated spanwise components of the different aspect ratios when the distributions are scaled by wingspan. The centrifugal, pressure gradient and total dynamic forces show a mostly outboard-directed (positive) distribution across the span, while the Coriolis net effect is comparable in magnitude but is directed inboard (negative) across the entirety of the wing. The sectional pressure gradient force is directed outboard along much of the span, but does switch sign on either end of the wing due to the interactions of the LEV with the root and tip vortices. The pressure gradient force is, again, shown to be the major contributor to the total dynamic force.

The integrated surface-normal forces (figure 12*b*) reveal an upward (positive) net force from the Coriolis across the span for each aspect ratio. The sectional pressure gradient and total dynamic forces have a net effect directed downward (negative) initially near the wing root for all aspect ratios. The total dynamic force remains negative until 81, 51 and 31 % span locations for the $AR = 1$, 2 and 4, respectively. The physical distances of the switch-over point correspond to 0.81, 1.02 and 1.25 chords from the wing root. The contribution of the surface-normal force continues to rise until reaching a maximum at 0.96, 1.71 and 2.10 chords, respectively, for each

https://doi.org/10.1017/jfm.2014.212 Published online by Cambridge University Press

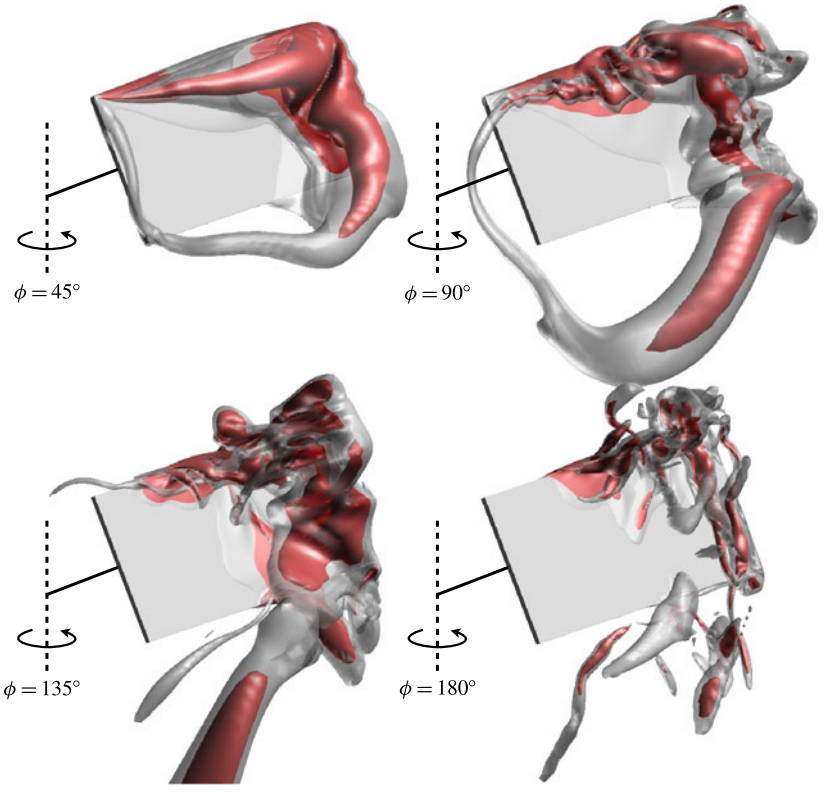


FIGURE 13. Evolution of the vortex structure about the revolving wing in the absence of centrifugal force.

span. This distance appears to saturate with aspect ratio, indicating that the LEV development may be reaching a critical Reynolds number along the span, which will promote the feeding sheet substructures discussed earlier. Since the centrifugal force is oriented radially, its integrated surface-normal component on each spanwise plane is non-zero, but negligible.

5.4. *Isolation of dynamic effects due to rotation*

In an attempt to separate and quantify the dominant mechanisms of LEV attachment, the aspect-ratio-two wing ($AR = 2$) is simulated with the addition of a source term in the governing equations to oppose and eliminate the centrifugal force, $\boldsymbol{F}_{cen} = -\rho\, \boldsymbol{\Omega} \times (\boldsymbol{\Omega} \times \boldsymbol{r})$, around the wing. This is in an effort to assess the importance of the centrifugal force to vortex attachment for revolving wings. The wing is revolved in the same manner as before, but the inboard oriented source term eliminates the contribution of the outboard centrifugal force around the wing. While this simulation cannot be represented by a physical experiment, it does provide a means of isolating effects of rotation to emphasize their importance.

Isosurfaces of relative total pressure are depicted in figure 13 for the wing without centrifugal force to highlight the overall vortex structure and the inner core at rotational angles $\phi = 45$, 90, 135 and 180°. For $\phi \leqslant 45°$, the flow field develops almost identically to the previous simulation when the centrifugal force is included.

https://doi.org/10.1017/jfm.2014.212 Published online by Cambridge University Press

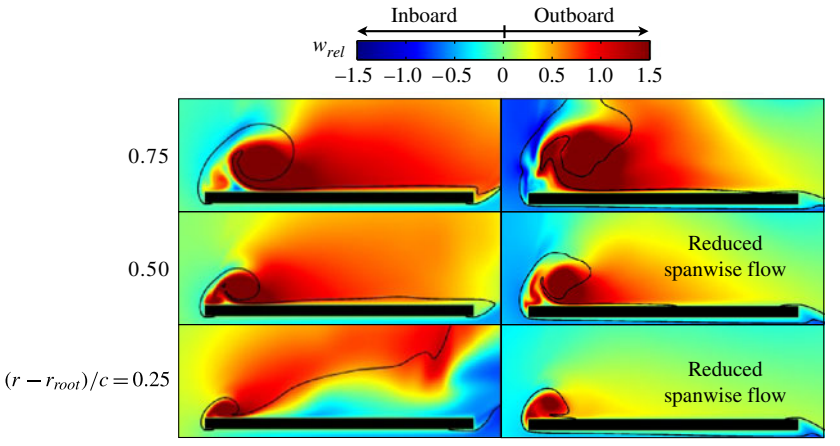


FIGURE 14. Relative spanwise velocity contours from the original solution and a solution with the centrifugal force eliminated. The rotational angle is $\phi = 90°$, and a single contour of total pressure is superimposed to highlight the LEV.

This is not surprising since the wing is accelerating up until this point and has not reached its constant rotational rate, indicating that the initial vortex formation and development is due to the acceleration of the wing. The leading-edge, tip and root vortices produced at the edges unpin from the outboard corners and reconnect as before. The leading-edge portion of the vortex lifts off the surface past midspan as it reorients itself with the wing tip. At $\phi = 90°$, however, the flow field starts to show differences. Without the outboard-directed centrifugal force, the lifted-off section of the LEV progresses inboard causing spiraling undulations of the core near the wing root. The root vortex also moves towards the rotational axis and separates from the wing. For $\phi > 90°$, the root vortex and the separated portion of the LEV continue to move inboard and eventually cause the entire vortex system to eject from the wing surface. At $\phi = 180°$, only remnants of the vortex system are evident around the wing.

The relative spanwise velocities from the original solution and a solution with the absence of centrifugal force are depicted at several spanwise locations in figure 14. The rotational angle is $\phi = 90°$. While there is a strong outboard flow present in the core of the LEV for both solutions, there is also a large inboard flow ahead of the leading edge in the absence of centrifugal force, which leads to increased shearing in the feeding sheet of the LEV. In addition, the region of outboard flow present behind the LEV in the chordwise direction is dramatically reduced in size and strength without the centrifugal force. This decreased spanwise flow around the vortex could lead to its eventual separation from the wing.

6. Summary and conclusions

A high-fidelity numerical study has been conducted to examine the vortex structure and aerodynamic loading on unidirectionally revolving wings. Several aspect ratios ($AR = 1$, 2 and 4) were considered at root-based Reynolds numbers of 1000. In all cases, four edge vortices that were anchored at the wing corners were generated after the onset of the motion. The mid-sections of those structures progressed into the wake while still pinned at the ends resulting in an arch-like lift-off of the LEV

https://doi.org/10.1017/jfm.2014.212 Published online by Cambridge University Press

near the wingtip. Eventually, the leading-edge, tip and trailing-edge vortices all unpinned from their respective outboard corners and connected into a continuous loop with the LEV portion remaining attached to the wing surface across much of the span and throughout the motion. The close proximity of the vortex to the wing promoted a strong and persistent region of suction that was maintained past midspan regardless of aspect ratio. Near the tip, the imprint of the LEV on the surface pressure diminished as it lifted away from the surface and reoriented along the chord through its connection with the tip vortex. The size of the vortex loop increases with aspect ratio since the travel distance at the wingtip also scales with span, but the overall development of the vortex system is similar for each aspect ratio. Although the wing used in this study was a simple rectangular planform, similar flow features have been observed by Harbig *et al.* (2013) for a completely different planform of a fruit fly wing, which highlights the robustness of these flows.

The $AR = 4$ wing promoted the development of substructures in the LEV feeding sheet; the origins of which were correlated to the local span-based Reynolds number achieved during rotation. For the fixed root-based Reynolds number examined, the lower-aspect-ratio wings did not have sufficient spans for these transitional elements to manifest. In contrast, vortex breakdown, which was encountered around midspan for each aspect ratio, appeared to be independent of the local Reynolds number and, instead, showed a stronger dependence on the established spanwise pressure gradient as described by Maxworthy (2007) between the root and tip of the wing. It is of interest to highlight that the independent causes of vortex breakdown and the shear-layer substructures parallels quite closely with what has been observed in the attached LEV formed over a swept delta wing: vortex breakdown is dependent upon the established pressure gradient between the apex and trailing edge, and substructures form as a result of the local length-based Reynolds number along the wing. This important relationship between rotating wings and swept delta wings can be extremely valuable for the continued understanding of flapping wing dynamics.

In addition, the LEV grew almost proportionally to the distance from the wing root, so its chordwise extent eventually became constrained by the trailing edge with increased aspect ratio, leading to a saturation of the aerodynamic loads. This geometric constraint indicates that, for the geometry and kinematics studied here, there is no advantage of increasing aspect ratio once the extent of the LEV occupies the entire chord of the wing, which happens to be around $AR = 2$. With $AR = 1$, the edge of the vortex never reaches the trailing edge, which allows the vortex to continue to grow slightly during rotation leading to a gradual rise of the aerodynamic loads throughout the motion.

The size and shear-layer development of the LEV were shown to be sensitive to the distance from the root of the wing, indicating that a Reynolds number based on spanwise position may be appropriate for comparisons of wings of differing aspect ratio as was similarly suggested by Harbig *et al.* (2013). Matching of the root-based Reynolds numbers between different wing planforms ensures that the variation of Reynolds number along the span is kept consistent, which is much like the scaling used for swept delta wings.

The centrifugal, Coriolis and pressure gradient forces were analysed for each of the different aspect ratio wings in and around the LEV. The normal and spanwise components of the pressure gradient force at the 25 % span location were shown to dominate the other two forces by an order of magnitude in the core of the LEV regardless of aspect ratio. However, the centrifugal force was found to be equally important outside the vortex core, and the two forces, together, were responsible for

https://doi.org/10.1017/jfm.2014.212 Published online by Cambridge University Press

the large regions of outboard flow above the wing. The normal component of the the Coriolis force was observed to be directed away from the wing surface at the base and in the core of the LEV indicating that it does not promote attachment of the vortex system, but rather, the opposite regardless of aspect ratio. The established outboard spanwise flow induced by the centrifugal and pressure gradient forces is believed to act like the convecting velocity over a swept-delta wing that prevents the separation at the tip from propagating inboard and allows for the sustained attachment of the LEV.

Finally, As a means of isolating dynamic effects due to rotation on LEV attachment, the $AR = 2$ wing was simulated with the addition of a source term in the governing equations to oppose and eliminate the centrifugal force near the wing surface. The initial formation and development of the LEV was unhindered by the absence of this force; however, later in the motion, the separation of the LEV near the tip was able to propagate inboard. Without the opposing outboard centrifugal force to keep the separation past midspan, the vortex eventually lifted away from the surface much like that of a translating wing undergoing stall. The relative spanwise velocity revealed a reduction of outboard flow between the LEV and the trailing edge and a strong region of inboard flow ahead of the leading edge when the centrifugal force was eliminated. The result is increased spanwise shearing of the vortex and eventual destabilization and lift-off of the entire system. These findings further the claims first proposed by Ellington *et al.* (1996) that spanwise flow transports vorticity to the tip and, thus, inhibits LEV growth.

Acknowledgements

This work was supported in part by AFOSR under a task monitored by Dr D. Smith and also by a grant of HPC time from the DoD HPC Shared Resource Centers at AFRL and ERDC.

REFERENCES

ALPERT, P. 1981 Implicit filtering in conjunction with explicit filtering. *J. Comput. Phys.* **44** (1), 212–219.

ANSARI, S., PHILLIPS, N., STABLER, G., WILKINS, P. C., ŻBIKOWSKI, R. & KNOWLES, K. 2009 Experimental investigation of some aspects of insect-like flapping flight aerodynamics for application to micro air vehicles. *Exp. Fluids* **46**, 777–798.

BEAM, R. & WARMING, R. 1978 An implicit factored scheme for the compressible Navier–Stokes equations. *AIAA J.* **16** (4), 393–402.

BIRCH, J. & DICKINSON, M. 2003 The influence of wing-wake interactions on the production of aerodynamic forces in flapping flight. *J. Expl Biol.* **206**, 2257–2272.

BIRCH, J., DICKSON, W. & DICKINSON, M. 2004 Force production and flow structure of the leading edge vortex on flapping wings at high and low Reynolds numbers. *J. Expl Biol.* **207**, 1063–1072.

CARR, Z. R., CHEN, C. & RINGUETTE, M. J. 2013 Finite-span rotating wings: three-dimensional vortex formation and variations with aspect ratio. *Exp. Fluids* **54** (2), 1–26.

CHENG, B., SANE, S. P., BARBERA, G., TROOLIN, D. R., STRAND, T. & DENG, X. 2013 Three-dimensional flow visualization and vorticity dynamics in revolving wings. *Exp. Fluids* **54**, 1423.

DICKINSON, M. 1994 The effects of wing rotation on unsteady aerodynamic performance at low Reynolds numbers. *J. Expl Biol.* **192**, 179–206.

ELDREDGE, J., WANG, C. & OL, M. 2009 A computational study of a canonical pitch-up, pitch-down, wing maneuver. *AIAA Paper* 2009-3687. AIAA.

https://doi.org/10.1017/jfm.2014.212 Published online by Cambridge University Press

ELLINGTON, C. 1999 The novel aerodynamics of insect flight: applications to micro-air vehicles. *J. Expl Biol.* **202**, 3439–3448.

ELLINGTON, C., VAN DEN BERG, C., WILLMOTT, A. P. & THOMAS, A. L. R. 1996 Leading-edge vortices in insect flight. *Nature* **384**, 626–630.

GAITONDE, D. & VISBAL, M. 1998 High-order schemes for Navier–Stokes equations: algorithm and implementation into FDL3DI. *Technical Report* AFRL-VA-WP-TR-1998-3060. Air Force Research Laboratory, Wright-Patterson AFB.

GAITONDE, D. & VISBAL, M. 1999 Further development of a Navier–Stokes solution procedure based on higher-order formulas. *AIAA Paper* 99-0557. AIAA.

GARMANN, D., VISBAL, M. & ORKWIS, P. 2013*a* Comparative study of implicit and subgrid-scale model large-eddy simulation techniques for low-Reynolds number airfoil applications. *Intl J. Numer. Meth. Fluids* **71** (12), 1546–1565.

GARMANN, D., VISBAL, M. & ORKWIS, P. 2013*b* Three-dimensional flow structure and aerodynamic loading on a revolving wing. *Phys. Fluids* **25**, 034101.

GORDNIER, R. E. & VISBAL, M. R. 1993 Numerical simulation of delta-wing roll. *AIAA Paper* 1993-0554. AIAA.

HARBIG, R. R., SHERIDAN, J. & THOMPSON, M. C. 2013 Reynolds number and aspect ratio effects on the leading-edge vortex for rotating insect wing planforms. *J. Fluid Mech.* **717**, 166–192.

JAMESON, A., SCHMIDT, W. & TURKEL, E. 1981 Numerical solutions of the Euler equations by finite volume methods using Runge–Kutta time stepping schemes. *AIAA Paper* 1981-1259. AIAA.

KIM, D. & GHARIB, M. 2010 Experimental study of three-dimensional vortex structures in translating and rotating plates. *Exp. Fluids* **49**, 329–339.

LEHMANN, F. 2004 The mechanisms of lift enhancement in insect flight. *Naturwissenschaften* **91**, 101–122.

LEHMANN, F. & PICK, S. 2007 The aerodynamic benefit of wing–wing interaction depends on stroke trajectory in flapping insect wings. *J. Expl Biol.* **210**, 1362–1377.

LELE, S. 1992 Compact finite difference schemes with spectral-like resolution. *J. Comput. Phys.* **103** (1), 16–42.

LENTINK, D. & DICKINSON, M. H. 2009*a* Biofluiddynamic scaling of flapping, spinning and translating fins and wings. *J. Expl Biol.* **212**, 2691–2704.

LENTINK, D. & DICKINSON, M. 2009*b* Rotational accelerations stabilize leading edge vortices on revolving fly wings. *J. Expl Biol.* **212**, 2705–2719.

MAO, S. & JIANGHAO, W. 2004 Large aerodynamic forces on a sweeping wing at low Reynolds number. *Acta Mechanica Sin.* **20** (1), 24–31.

MATTHEW, J., LECHNER, R., FOYSI, H., SESTERHENN, J. & FRIEDRICH, R. 2003 An explicit filtering method for LES of compressible flows. *Phys. Fluids* **15** (8), 2279–2289.

MAXWORTHY, T. 2007 The formation and maintenance of a leading-edge vortex during the forward motion of an animal wing. *J. Fluid Mech.* **587**, 471–475.

OZEN, C. & ROCKWELL, D. 2012*a* Flow structure on a rotating plate. *Exp. Fluids* **52** (1), 207–223.

OZEN, C. A. & ROCKWELL, D. 2012*b* Three-dimensional flow structure on a rotating wing. *J. Fluid Mech.* **707**, 541–550.

POELMA, C., DICKSON, W. & DICKINSON, M. 2006 Time-resolved reconstruction of the full velocity field around a dynamically-scaled flapping wing. *Exp. Fluids* **41**, 213–225.

PULLIAM, T. 1986 Artificial dissipation models for the Euler equations. *AIAA J.* **24** (12), 1931–1940.

PULLIAM, T. & CHAUSSEE, D. 1981 A diagonal form of an implicit approximate-factorization algorithm. *J. Comput. Phys.* **17** (10), 347–363.

RIZZETTA, D. P., VISBAL, M. R. & MORGAN, P. E. 2008 A high-order compact finite-difference scheme for large-eddy simulation of active flow control (invited). *AIAA Paper* 2008-526. AIAA.

SANE, S. 2003 The aerodynamics of insect flight. *J. Expl Biol.* **206** (23), 4191–4208.

SHYY, W., AONO, H., KANG, C. & LIU, H. 2013 *An Introduction to Flapping Wing Aerodynamics*. Cambridge University Press.

SHYY, W., LIAN, Y., TANG, J., VIIERU, D. & LIU, HAO. 2008 *Aerodynamics of Low Reynolds Number Flyers*. Cambridge University Press.

https://doi.org/10.1017/jfm.2014.212 Published online by Cambridge University Press

STOLZ, S. & ADAMS, N. 1999 An approximate deconvolution procedure for large-eddy simulation. *Phys. Fluids* **11** (7), 1699–1701.

TANNEHILL, J. C., ANDERSON, D. A. & PLETCHER, R. H. 1997 *Computational Fluid Mechanics and Heat Transfer*, 2nd edn Series in Computational and Physical Processes in Mechanics and Thermal Sciences. Taylor & Francis.

USHERWOOD, J. R. & ELLINGTON, C. 2002*a* The aerodynamics of revolving wings: I. Model hawkmoth wings. *J. Expl Biogr.* **205**, 1547–1564.

USHERWOOD, J. R. & ELLINGTON, C. 2002*b* The aerodynamics of revolving wings: II. Propeller force coefficients from mayfly to quail. *J. Expl Biogr.* **205**, 1565–1576.

VISBAL, M. 1994 Onset of vortex breakdown above a pitching delta wing. *AIAA J.* **32** (8), 1568–1575.

VISBAL, M. R. & GAITONDE, D. V. 1999 High-order accurate methods for complex unsteady subsonic flows. *AIAA J.* **37** (10), 1231–1239.

VISBAL, M. R. & GAITONDE, D. V. 2002 On the use of high-order finite-difference schemes on curvilinear and deforming meshes. *J. Comput. Phys.* **181**, 155–185.

VISBAL, M. & GORDNIER, R. 2003 On the structure of the shear layer emanating from a swept leading edge at angle of attack. *AIAA Paper* 2003-4016. AIAA.

VISBAL, M. R., MORGAN, P. E. & RIZZETTA, D. P. 2003 An implicit LES approach based on high-order compact differencing and filtering schemes. *AIAA Paper* 2003-4098. AIAA.

VISBAL, M. R. & RIZZETTA, D. P. 2002 Large-eddy simulation on curvilinear grids using compact differencing and filtering schemes. *Trans. ASME J. Fluids Engng* **124**, 836–847.

https://doi.org/10.1017/jfm.2014.212 Published online by Cambridge University Press